J. Fluid Mech. (2007), *vol.* 586, *pp.* 83–108.
doi:10.1017/S0022112007007082 Printed in the United Kingdom

Stratified turbulence forced in rotational and divergent modes

E. LINDBORG AND G. BRETHOUWER

Linné Flow Center, Department of Mechanics, KTH, SE-100 44 Stockholm, Sweden

(Received 9 October 2006 and in revised form 30 April 2007)

We perform numerical box simulations of strongly stratified turbulence. The equations solved are the Boussinesq equations with constant Brunt–Väisälä frequency and forcing either in rotational or divergent modes, or, with another terminology, in vortical or wave modes. In both cases, we observe a forward energy cascade and inertial-range scaling of the horizontal kinetic and potential energy spectra. With forcing in rotational modes, there is approximate equipartition of kinetic energy between rotational and divergent modes in the inertial range. With forcing in divergent modes the results are sensitive to the vertical forcing wavenumber k_v^f. If k_v^f is sufficiently large the dynamics is very similar to the dynamics of the simulations which are forced in rotational modes, with approximate equipartition of kinetic energy in rotational and divergent modes in the inertial range. Frequency spectra of rotational, divergent and potential energy are calculated for individual Fourier modes. Waves are present at low horizontal wavenumbers corresponding to the largest scales in the boxes. In the inertial range, the frequency spectra exhibit no distinctive peaks in the internal wave frequency. In modes for which the vertical wavenumber is considerably larger than the horizontal wavenumber, the frequency spectra of rotational and divergent modes fall on top of each other. The simulation results indicate that the dynamics of rotational and divergent modes develop on the same time scale in stratified turbulence. We discuss the relevance of our results to atmospheric and oceanic dynamics. In particular, we review a number of observational reports indicating that stratified turbulence may be a prevalent dynamic process in the ocean at horizontal scales of the order of 10 or 100 m up to several kilometres.

1. Introduction

There has been significant progress during recent years in the understanding of strongly stratified flows. A relatively simple, yet important, idea in the conceptual development is to introduce two different Froude numbers (Billant & Chomaz 2001) to characterize different flows, the vertical and the horizontal Froude numbers, defined as

$$F_v = \frac{u}{N l_v}, \quad F_h = \frac{u}{N l_h}, \tag{1.1}$$

where N is the Brunt–Väisälä frequency, u is a characteristic velocity and l_v and l_h are the characteristic vertical and horizontal length scales, respectively. Traditionally, strength of stratification has been measured by the inverse of the vertical Froude number and much of the theoretical framework for strongly stratified flows has been developed for the limit $F_v \to 0$. A central part of this framework is the vortical–wave decomposition (see Riley & Lelong 2000 for a review). Kinematically,

this decomposition is based on a Helmholtz decomposition of the horizontal velocity field into a rotational and a non-rotational part. The vertical velocity is added to the non-rotational part. Thus, we can write (Lelong & Riley 1991)

$$\boldsymbol{u} = \boldsymbol{e}_z \times \nabla_h \Psi + \{\nabla_h \Phi + w\boldsymbol{e}_z\}, \tag{1.2}$$

where Ψ is a stream function, Φ a velocity potential, $\boldsymbol{e}_z$ the vertical unit vector and w the vertical velocity component. The first term is horizontally non-divergent and carries all the vertical vorticity while the second, bracketed, term is vertically irrotational and carries all the horizontal divergence of the field. Therefore, we may call them the rotational and the divergent parts of the field, remembering that in doing so we are referring only to the horizontal direction. Dynamically, the vortical–wave decomposition is based on the assumption that there is a decoupling between the rotational and the divergent parts of the field in the limit of strong stratification, or more specifically in the limit $F_v \to 0$. This assumption can be justified by the introduction of two time scales (Lelong & Riley 1991): a slow advective time scale of the vortical dynamics and a fast time scale of the wave dynamics. These can be estimated as

$$T_{slow} \sim \frac{l_h}{u}, \quad T_{fast} \sim \frac{\sqrt{l_v^2 + l_h^2}}{N l_v} \sim \frac{l_h}{N l_v}, \tag{1.3}$$

where the estimate of the fast time scale is based on the dispersion relation for the internal gravity wave frequency and the assumption that $l_h \geqslant l_v$, typically. The ratio between the time scales can thus be estimated as

$$\frac{T_{fast}}{T_{slow}} \sim \frac{u}{N l_v} = F_v. \tag{1.4}$$

Introducing F_v as a small parameter and using the method of multiple time scales, it can be demonstrated that the dynamic equations for the rotational and the divergent parts of the velocity field decouple to lowest order. The equation for the divergent part is just the linear internal wave equation and the equation for the rotational part of the field is the equation for the vertical vorticity, either in its linear form (Lelong & Riley 1991) or its nonlinear form (Riley & Lelong 2000). In the next-order equations in the expansion, there are terms describing the interactions between the two fields. In the limit $F_v \to 0$, the dynamics can thus be decomposed into waves and vortices which are weakly interacting. A substantial amount of work has been done to describe the different types of interactions among waves and vortices (see Godeferd & Cambon 1994; Bartello 1995 and references therein).

In recent work, the focus has shifted from the limit $F_v \to 0$ to the limit $\{F_h \to 0,\ F_v \sim 1\}$. Billant & Chomaz (2001) carried out a similarity analysis of the inviscid Boussinesq equations, in which they introduced the ratio $\alpha = l_v/l_h$ as a free parameter whose asymptotic behaviour in the limit of strong stratification was determined from the analysis. They reduced the Boussinesq equations to a set of nonlinear equations which lose their explicit dependence on F_h as $F_h \to 0$, provided that $\alpha \sim F_h$. The last condition is equivalent to $F_v \sim 1$ as $F_h \to 0$. They argued that many flows in nature will obey this type of scaling by adjusting their vertical length scale so that $l_v \sim u/N$ as $F_h \to 0$. For a given velocity scale the vertical length scale will thus decrease as the strength of stratification is increased and the limit $F_v \to 0$ will never be reached, no matter how strong the stratification becomes. Riley & deBruynKops (2003) carried out direct numerical simulations of decaying stratified flows initialized with perturbed Taylor–Green vortices. They observed a rapid initial decrease of the vertical length scale consistent with the prediction of Billant &

Chomaz (2001). Waite & Bartello (2004) verified the prediction $l_v \sim u/N$ in numerical simulations of stratified turbulence forced in rotational modes with no vertical variation. Lindborg (2006) carried out a set of box simulations of stratified turbulence forced in rotational modes using successively thinner boxes and increased vertical resolution as F_h was decreased. The agreement with the Billant & Chomaz prediction was excellent. Moreover, it was demonstrated that there is a forward cascade of kinetic and potential energy in the limit of strong stratification, with horizontal kinetic and potential energy spectra of similar form to that in three-dimensional turbulence, that is

$$E_K(k_h) = C_1 \epsilon_K^{2/3} k_h^{-5/3}, \tag{1.5}$$

$$E_P(k_h) = C_2 \frac{\epsilon_P}{\epsilon_K^{1/3}} k_h^{-5/3}, \tag{1.6}$$

where ϵ_K and ϵ_P are the mean dissipation rates of kinetic and potential energy respectively and C_1 and C_2 are two constants corresponding to the Kolmogorov and Oboukhov–Corrsin constants of three-dimensional turbulence. Here, k_h, is the magnitude of the one-dimensional wavenumber, i.e. if the spectrum is measured in the x-direction, then $k_h = |k_x|$. Somewhat surprisingly, the two constants were found to take the same value, $C_1 = C_2 = 0.51$. Lindborg (2006) suggested that this type of stratified turbulence, found in the limit $\{F_h \to 0,\ F_v \sim 1\}$ and exhibiting inertial-range dynamics in the horizontal, can be the dynamic origin of the $k_h^{-5/3}$-range found in the mesoscale atmospheric energy spectra (Nastrom, Gage & Jasperson 1984). It was also demonstrated (Lindborg 2005) that the forward energy cascade of stratified turbulence can be observed in the presence of system rotation, provided that it is not too strong. In these simulations, hyperviscosity was used in order to reach the asymptotic state of inertial-range dynamics. Using Navier–Stokes viscosity in their direct numerical simulations Riley & deBruynKops (2003) observed a dynamics exhibiting inertial-range behaviour, with horizontal kinetic energy spectra in approximate accordance with (1.5). It was later confirmed (Jim Riley, private communication) that their potential energy spectra were also in approximate agreement with (1.6). Recently, Brethouwer *et al.* (2007) carried out a set of direct numerical simulations with Navier–Stokes viscosity and forcing in large-scale rotational modes. These simulations confirmed the Billant & Chomaz scaling analysis and also showed inertial-range dynamics.

The aforementioned simulations were either initialized (Riley & deBruynKops 2003) or forced (Waite & Bartello 2004; Lindborg 2005, 2006; Brethouwer *et al.* 2007) only in rotational modes. Interpreting these results in the light of the vortical–wave decomposition it would be tempting to conclude that the scaling $l_v \sim u/N$ and the forward energy cascade dynamics are properties of the vortical part of the field, but probably not of the wave part. However, this is questionable. The dynamic basis of the vortical–wave decomposition is the assumption of two fields which are only weakly interacting because they develop on two separate time scales whose ratio is of the order of $F_v \ll 1$, in accordance with (1.4). If $F_v \sim 1$ this basis is lost and there is no reason to believe that rotational and divergent modes should be dynamically decoupled, as also pointed out by Billant & Chomaz (2001). On the contrary, we can expect that the nonlinear interactions between rotational and divergent modes are so strong that a decomposition of the field would show no qualitative differences between the two types of modes when inertial-range quantities are considered. It can also be expected that it is not of crucial importance whether the forcing is applied in rotational or divergent modes, as long as it does not generate large-scale dynamics violating the condition $F_v \sim 1$. If a traditional type of phenomenology is applicable

to the inertial-range dynamics of stratified turbulence, these dynamics should not be strongly influenced by the forcing, but rather possess some degree of universality. In this paper, we will investigate this numerically.

2. Simulations

We perform box simulations of the Boussinesq equations in a non-rotating frame of reference:

$$\frac{\partial \boldsymbol{u}}{\partial t} + (\boldsymbol{u}\cdot\nabla)\boldsymbol{u} = -\nabla p + N\boldsymbol{e}_z\phi + D_u + \boldsymbol{f}, \tag{2.1}$$

$$\frac{\partial \phi}{\partial t} + (\boldsymbol{u}\cdot\nabla)\phi = -Nw + D_\phi, \tag{2.2}$$

$$\nabla\cdot\boldsymbol{u} = 0. \tag{2.3}$$

Here, $\boldsymbol{u}$ is the velocity field, D_u and D_ϕ are diffusion terms, p is the pressure, $\boldsymbol{f}$ is forcing, $\boldsymbol{e}_z$ is the vertical unit vector, N is the Brunt–Väisälä frequency, $\phi = gT'/(NT_o)$, where T' and T_o are the fluctuating and equilibrium potential temperatures, respectively, g is the acceleration due to gravity and $w = \boldsymbol{e}_z\cdot\boldsymbol{u}$ is the vertical velocity component.

The simulations are performed in a similar way to Lindborg (2006) but with a different code. The diffusion terms are set as

$$D_u = \left(-\nu_h\Delta_h^4 - \nu_v\frac{\partial^8}{\partial z^8}\right)\boldsymbol{u}, \quad D_\phi = \left(-\kappa_h\Delta_h^4 - \kappa_v\frac{\partial^8}{\partial z^8}\right)\phi, \tag{2.4}$$

where Δ_h is the horizontal Laplace operator, ν_h and κ_h are horizontal diffusion coefficients and ν_v and κ_v are vertical diffusion coefficients. The use of high-order hyperdiffusion with different diffusion coefficients in the vertical and horizontal directions limits the influence of viscosity to the very highest wavenumbers and allows us to use higher resolution in the vertical than in the horizontal direction. In all simulations the degree of stratification is strong, with $F_h \ll 1$, and in all simulations we use highly elongated boxes, since the ratio between the vertical and the horizontal length scales of the flows is much smaller than unity. One of the most important parameters is the vertical grid spacing Δz. Brethouwer *et al.* (2007) showed that a necessary condition for the appearance of stratified turbulence which is not strongly affected by viscous effects at vertical scale $l_v = u/N$ is that $l_O/\eta > 1$, where $l_O = \epsilon^{1/2}/N^{3/2}$ is the Ozmidov length scale and η is the Kolmogorov scale. This condition was derived from stratified turbulence theory and was also confirmed numerically. Since the Kolmogorov scale is to be resolved in a DNS, it is required that $\Delta z < l_O$ in a DNS of stratified turbulence. With hyperviscosity of the type which we employ in this study, Brethouwer *et al.* (2007, Appendix A) showed that it is sufficient that the vertical viscous length scale is of the order of the Ozmidov length scale or even somewhat larger for the appearance of stratified turbulence which is not strongly affected by viscous effects at vertical scale $l_v = u/N$. In accordance with this analysis we choose $\Delta z \approx 7l_O$. We apply this resolution criterion in all simulations.

A pseudospectral code with periodic boundary conditions in all three directions is employed. The time integration of the nonlinear terms is carried out using a fourth-order Runge–Kutta scheme and the viscous terms are exactly integrated. Aliasing errors are avoided by a combination of phase shifting and truncation, according to the method described by Canuto *et al.* (1988). The horizontal sides of the box are set so that $L_x = L_y = 2\pi$ and in each simulation we apply forcing either in rotational or

divergent modes. We call the simulations with forcing in rotational modes 'r-runs' and the simulations with forcing in divergent modes 'd-runs'. The forcing injects energy into the system at a rate $P = 1$. In r-runs the forcing scheme is the same as used by Brethouwer *et al.* (2007). Forcing is applied exclusively in modes for which $k_v = 0$ with initial fields having a random seed energy in modes for which $k_v \neq 0$. This procedure will lead to a spontaneous formation of layers whose thickness scales as $l_v \sim u/N$. The forcing has a two-dimensional spectrum with a sharp peak at $k_\rho^f = 3$, where $k_\rho = \sqrt{k_x^2 + k_y^2}$ is the two-dimensional horizontal wavenumber. Non-rotational modes for which $k_v = 0$ belong to a special case which is not of much interest in this study. The horizontal velocity and the horizontal divergence of horizontal velocity are zero in these modes. Forcing in these modes leads to the generation of linear internal waves with frequency N and all kinetic energy in the vertical velocity component. Energy will spread very slowly from these waves to other regions in Fourier space.

When forcing is applied in divergent modes we therefore choose to force in modes for which $k_v \neq 0$. This makes a crucial difference between r-runs and d-runs. In r-runs the vertical length scale which develops in the flow will adjust so that $F_v \sim 1$. In d-runs, on the other hand, a vertical length scale $l_v = 2\pi/k_v^f$ is imposed on the flow and if it is much larger than u/N we can no longer expect that the flow will reach a state for which $F_v \sim 1$. Therefore we will choose $k_v^f \gg k_\rho^f$, because our aim is to investigate the dynamics in the limit $\{F_h \to 0, F_v \sim 1\}$. Thus, the d-runs are not designed to investigate whether a state for which $\{F_h \to 0, F_v \sim 1\}$ spontaneously develops from a completely different state, but rather to investigate whether forcing in divergent modes for which $k_v^f \gg k_\rho^f$ will give the same type of dynamics as with forcing in rotational modes. The internal gravity wave fields in the atmosphere and the oceans are dominated by waves with much larger horizontal than vertical wavelengths (see e.g. Dewan 1997 and references therein for atmospheric data and e.g. Garret & Munk 1975 for oceanic data). In a rudimentary way, the choice $k_v^f \gg k_\rho^f$ therefore mimics a state which is not too far from what we can expect to see in nature. It should also be noted that the fixed value of k_v^f with $k_v^f \gg k_\rho^f$ does not mean that F_v is prescribed during the whole simulation. It only means that we choose an initial value of F_v which is not too far from unity. In this respect there is an important difference between the simulations presented in this paper and those carried out by Waite & Bartello (2006), who studied stratified turbulence forced in wave modes for which $k_v^f = k_\rho^f$. In d-runs we vary the vertical forcing wavenumber k_v^f from run to run, while we always force in the horizontal wavenumber band $k_\rho \in [1\ 5]$, where we define the typical horizontal forcing wavenumber as $k_\rho^f = 3$. In the Appendix we give a complete description of the forcing scheme.

The simulations are listed in table 1. We divide them into six sets called A, B, C, D, E and F. In each of these sets one r-run (for example Ar) and one or several d-runs (for example Ad1, Ad2, Ad3 and Ad4) are carried out. The end state from the r-run is used as the initial state for each of the d-runs. The only parameter which is varied between the d-runs in each set is the vertical forcing wavenumber k_v^f. In the set of A-runs one additional run, $\mathrm{Ar_{ex}}$, is carried out with forcing in rotational modes. In this run we have extended the height of the box by a factor of eight compared to the Ar-run, leaving all other parameters unchanged. Run $\mathrm{A_{ex}}$ will be discussed in § 3.1.

3. Results

The r-runs show very similar dynamics to the simulations by Lindborg (2006). A stationary state is reached quite fast, in which the energy injected at large horizontal

Run	F_h	F_v	Ri	k_v'	$\frac{L_x P(k_v^f)^3}{N^3}$	$\frac{E_P}{E_K}$	$\frac{\varepsilon_P}{\varepsilon_K}$	$\frac{L_x}{L_z}$	$N_x \times N_z$	$\frac{\Delta z}{l_O}$	$\nu_h = \kappa_h$	$\nu_v = \kappa_v$
Ar	4.3×10^{-2}		1.2			0.09	0.32	16	256×64	7.1	1.5×10^{-13}	6.0×10^{-18}
Ar_{ex}	5.4×10^{-2}		1.3			0.14	0.34	2	256×512	7.2	1.5×10^{-13}	6.0×10^{-18}
Ad1	9.2×10^{-2}	0.5	1.0	1	0.03	0.17	0.47	16	256×64	7.8	1.5×10^{-13}	6.0×10^{-18}
Ad2	7.0×10^{-2}	1.1	1.2	3	0.69	0.14	0.51	16	256×64	7.7	1.5×10^{-13}	6.0×10^{-18}
Ad3	3.6×10^{-2}	0.9	1.8	5	3.2	0.42	0.59	16	256×64	6.8	1.5×10^{-13}	6.0×10^{-18}
Ad4	1.9×10^{-2}	0.9	1.7	9	18.8	0.26	0.25	16	256×64	6.8	1.5×10^{-13}	6.0×10^{-18}
Br	6.5×10^{-2}		2.1			0.15	0.45	10	384×48	7.4	8.0×10^{-15}	1.5×10^{-15}
Bd1	1.9×10^{-1}	0.6	0.9	1	0.03	0.11	0.46	10	384×48	8.8	8.0×10^{-15}	1.5×10^{-15}
Bd2	9.0×10^{-2}	0.9	1.3	3	0.79	0.13	0.50	10	384×48	7.5	8.0×10^{-15}	1.5×10^{-15}
Bd3	4.6×10^{-2}	0.8	2.5	5	3.6	0.47	0.59	10	384×48	7.7	8.0×10^{-15}	1.5×10^{-15}
Cr	1.6×10^{-2}		0.9			0.13	0.35	40	384×96	7.1	8.0×10^{-15}	3.7×10^{-22}
Cd1	3.1×10^{-2}	0.4	1.2	1	0.03	0.32	0.52	40	384×96	7.9	8.0×10^{-15}	3.7×10^{-22}
Cd2	2.7×10^{-2}	1.1	1.0	3	0.79	0.16	0.46	40	384×96	7.5	8.0×10^{-15}	3.7×10^{-22}
Cd3	1.7×10^{-2}	1.1	1.2	5	3.6	0.27	0.49	40	384×96	7.4	8.0×10^{-15}	3.7×10^{-22}
Cd4	9.5×10^{-3}	1.0	1.0	8	14.9	0.29	0.42	40	384×96	7.3	8.0×10^{-15}	3.7×10^{-22}
Dr	3.6×10^{-3}		0.7			0.09	0.32	256	1024×128	7.1	7.2×10^{-18}	6.5×10^{-29}
Dd1	4.4×10^{-3}	0.4	1.3	1	0.11	0.62	0.51	256	1024×128	8.2	7.2×10^{-18}	6.5×10^{-29}
Dd2	3.2×10^{-3}	1.1	0.8	3	2.9	0.44	0.42	256	1024×128	7.4	7.2×10^{-18}	6.5×10^{-29}
Dd3	2.8×10^{-3}	1.0	0.8	4	6.8	0.41	0.39	256	1024×128	7.1	7.2×10^{-18}	6.5×10^{-29}
Er	1.8×10^{-2}		1.3			0.15	0.46	32	1024×128	5.3	7.2×10^{-18}	2.5×10^{-22}
Ed	1.4×10^{-2}	0.7	1.3	5	3.2	0.53	0.53	32	1024×128	5.4	7.2×10^{-18}	2.5×10^{-22}
Fr	1.2×10^{-2}		0.8			0.11	0.34	196	512×32	6.7	7.8×10^{-16}	7.0×10^{-24}
Fd	1.2×10^{-2}	0.8	0.9	1	1.4	0.32	0.45	196	512×32	6.9	7.8×10^{-16}	7.0×10^{-24}

TABLE 1. Overview of the numerical and physical parameters used in the simulations. Ri is the Richardson number defined by (4.1), k_v' is the normalized forced vertical wavenumber defined by (3.2), E_P/E_K is the mean ratio of potential to kinetic energy, L_x/L_z is the ratio of the horizontal to vertical domain size, and N_x and N_z are the number of modes in the horizontal respectively vertical direction.

scales cascades to the very smallest scales where it is dissipated, leading to a balance between power input and mean dissipation. There is a spontaneous formation of layers whose thickness scales as $l_v \sim u/N$, in accordance to the Billant & Chomaz (2001) analysis. This is reflected in figure 1(*a*), showing a horizontal velocity component in a vertical plane from run Cr. Since the forcing has no vertical variation the layered structure in this particular figure is the result of the inherent dynamics of the Boussinesq equations.

The one-dimensional normalized and compensated horizontal spectra of kinetic and potential energy from some of the r-runs are plotted in figure 2. All the spectra show a rather clean inertial range in accordance with (1.5) and (1.6). However, the spectra from the simulations with strongest stratification and most grid points exhibit bottlenecks, a phenomenon which was not generally observed in the simulations by Lindborg (2006). The bottleneck is the 'bump' seen between the $k_h^{-5/3}$-range and the dissipation range where the spectrum falls off exponentially. Such a bottleneck is also found in the kinetic energy spectrum of isotropic Navier–Stokes turbulence (see e.g. Kaneda *et al.* 2003). It has been demonstrated (Lamorgese, Caughey & Pope 2005) that the bottleneck is magnified when hyperviscosity is used instead of Navier–Stokes viscosity and with higher-order hyperviscosity the bottleneck tends to be larger. In the case of a narrow inertial range the slope of the energy spectrum and

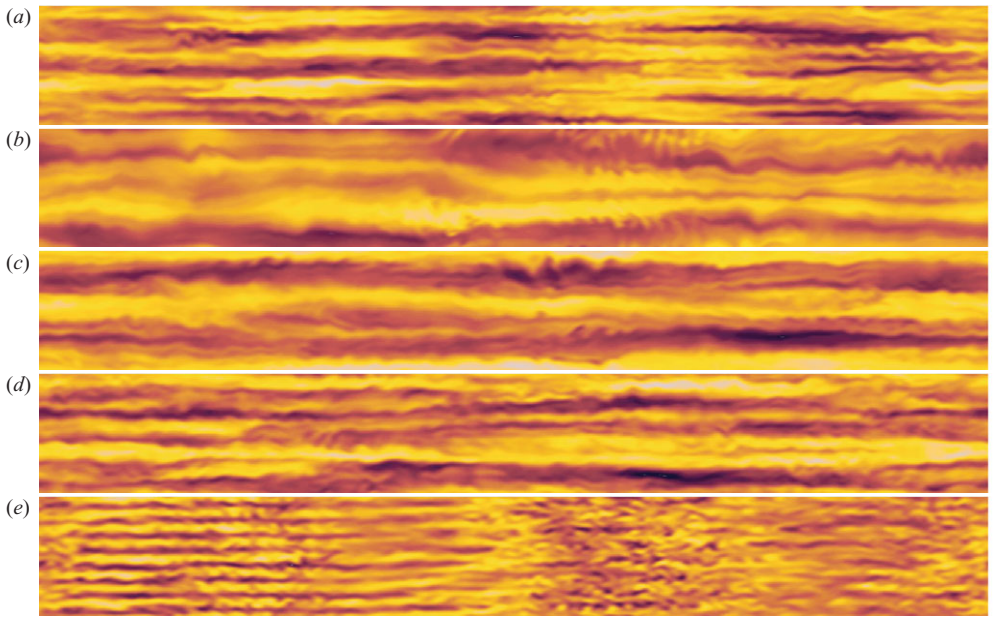

FIGURE 1. Snapshots of the horizontal velocity in a vertical plane. (*a*) run Cr, (*b*) Cd1, (*c*) Cd2, (*d*) Cd3, (*e*) Cd4. The vertical dimension is stretched by a factor of five.

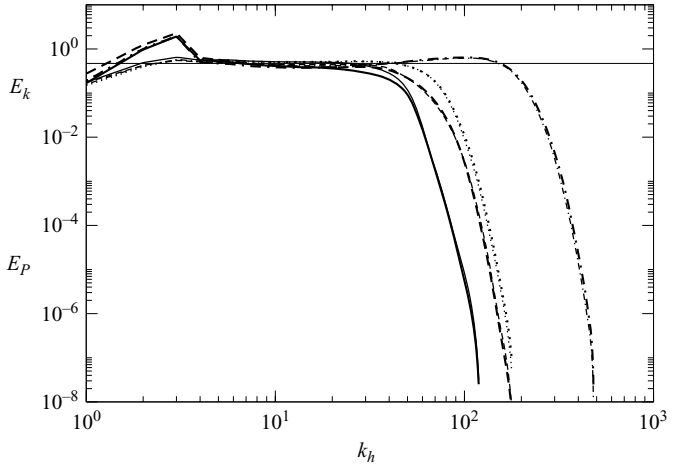

FIGURE 2. The compensated horizontal one-dimensional kinetic energy spectra $E_K(k_h)k_h^{5/3}/\varepsilon_K^{2/3}$ (thick lines) and potential energy spectra $E_P(k_h)k_h^{5/3}\varepsilon_K^{1/3}/\varepsilon_P$ (thin lines). ———, Ar; – – –, Br; · · · · ·, Cr; —·—·—, Dr. Straight line: $C_1 = C_2 = 0.47$.

the Kolmogorov constant will be slightly different between simulations with different orders of hyperviscosity. In our case, there may be several different parameters apart from the hyperviscosity determining the size of the bottleneck, such as the ratio between the vertical and horizontal resolution scale and the degree of stratification. In this study, we will not investigate this phenomenon further. As long as we use hyperviscosity we have to disregard the bottleneck as an anomalous result. The constants C_1 and C_2 are generally found to take approximately the same value in

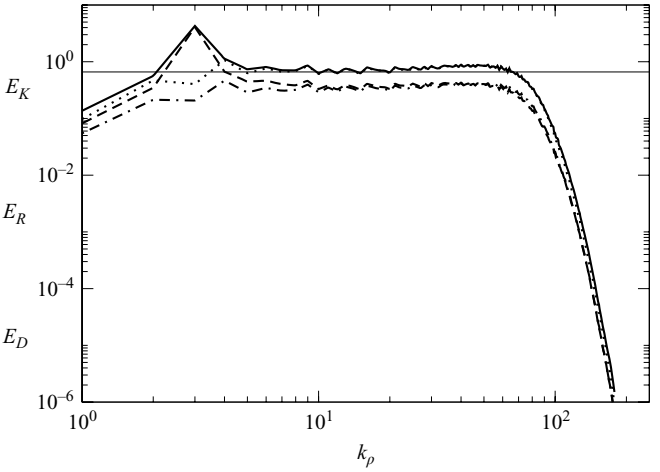

FIGURE 3. The compensated horizontal two-dimensional spectra, extracted from run Cr, of the kinetic energy $E_K(k_h)k_h^{5/3}/\varepsilon_K^{2/3}$ ———, rotational energy $E_R(k_h)k_h^{5/3}/\varepsilon_K^{2/3}$ – – –, divergent energy $E_D(k_h)k_h^{5/3}/\varepsilon_K^{2/3}$ —·—·— and potential energy $E_P(k_h)k_h^{5/3}\varepsilon_K^{1/3}/\varepsilon_P$ · · · · ·. Straight line: $C_1 = C_2 = 0.66$.

each simulation, so that the normalized potential and kinetic energy spectra fall on top of each other. However, the value is generally a little lower than the value 0.51 calculated by Lindborg (2006). In figure 2 we have drawn the straight line $C_1 = C_2 = 0.47$ for comparison.

In order to decompose the kinetic energy spectrum into rotational and divergent parts, it is appropriate to consider the two-dimensional spectrum instead of the one-dimensional spectrum. If the one-dimensional spectrum displays a $k_h^{-5/3}$-range the same is true for the two-dimensional spectrum and the relation between the two constants is (see Lindborg 1999)†

$$C' = \frac{2^{2/3}\pi\Gamma\left(\frac{1}{3}\right)}{3^{3/2}\left(\Gamma\left(\frac{2}{3}\right)\right)^2}C \approx 1.40C, \tag{3.1}$$

where C' and C are the constants of the two-dimensional and one-dimensional spectra, respectively. The two-dimensional normalized and compensated kinetic and potential energy spectra from run Cr and run Dr are plotted in figures 3 and 4 respectively, where we also have decomposed the energy spectrum into the spectra of rotational and divergent modes. In these figures, we have also drawn the straight line $C_1' = C_2' = 0.66$ which is the value corresponding to $C_1 = C_2 = 0.47$. In the inertial range, the normalized kinetic and potential energy spectra fall on top of each other in each case. It should be noted, however, that this does not mean that there is equipartition between kinetic and potential energy in the inertial range. On the other hand, it means that the ratio, $E_P(k_\rho)/E_K(k_\rho)$, between the potential and kinetic energy spectra is equal to the ratio ϵ_P/ϵ_K, which is in the range [0.3 0.5] for the r-runs (see table 1). The rotational part of the kinetic energy spectrum shows a clear peak at the

† When we prepared this manuscript we discovered that there is a misprint in Lindborg (1999). The middle term in equation (50), relating the structure function Kolmogorov constant to the one-dimensional Kolmogorov constant, should be divided by 2π. This equation together with equation (52) in Lindborg (1999) give the relation (3.1).

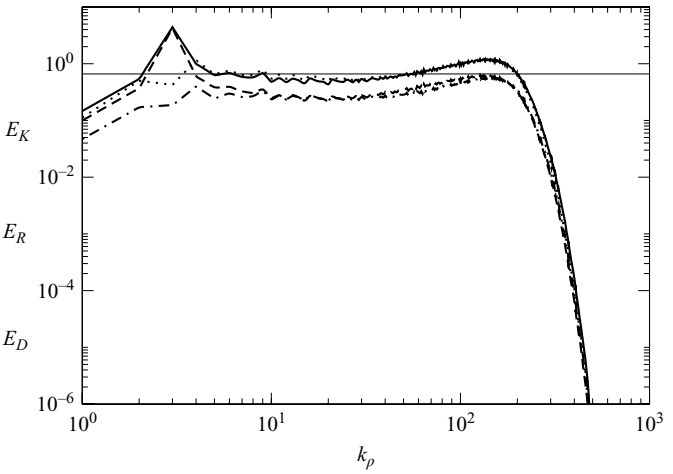

FIGURE 4. The compensated horizontal two-dimensional spectra, extracted from run Dr. Lines as in figure 3.

forcing wavenumber, reflecting the fact that energy is injected into rotational modes at this wavenumber. In the inertial range, the rotational and divergent parts of the kinetic energy spectra are almost equal in magnitude. This is a general observation for all r-runs. Since the energy is injected exclusively into rotational modes there must be a substantial energy transfer from rotational to divergent modes at scales comparable to the injection scale and in the inertial range the dynamics has reached an equilibrium with approximate equipartition of kinetic energy between rotational and divergent modes. This clearly indicates that the two types of modes are not dynamically decoupled from each other. A more reasonable interpretation is that there is a single type of dynamics giving rise to the two spectra.

We now turn to the d-runs. It was found that the evolution of these runs was very sensitive to variations of the vertical forcing wavenumber k_v^f. The time evolution of kinetic and potential energy is plotted in figure 5 for the Ad-runs and the Cd-runs. In figure 5 and the figures thereafter, the time is normalized by $P^{-1/3}l_h^{2/3}$, where P is the power input by the forcing and $l_h = 2\pi/k_\rho^f$. The curves from the two sets of runs are very similar and the simulations from the other sets also showed very similar curves. To simplify the presentation we introduce the normalized vertical forcing wavenumber

$$k_v' = k_v^f \frac{L_z}{L_x}. \tag{3.2}$$

When forcing is applied at the smallest non-zero vertical wavenumber in the box, $k_v' = 1$, there is a substantial initial growth of both kinetic and potential energy. The energy curves also oscillate with a rather well-defined frequency. In all d-runs with forcing at $k_v' = 1$ these oscillations were present, suggesting that internal gravity waves of a particular frequency were excited. Indeed, a Fourier analysis of the time series showed a very sharp peak at a particular frequency for each of these runs. Assuming that the vertical wavelength of the excited wave corresponds to the vertical forcing wavenumber one can determine the corresponding horizontal wavenumber by using the dispersion relation for internal gravity waves. In all these cases we determine the horizontal wavenumber of the internal wave as $k_\rho \approx 1.1$. In other words, waves are excited at the smallest non-zero horizontal wavenumbers in the box. None of the

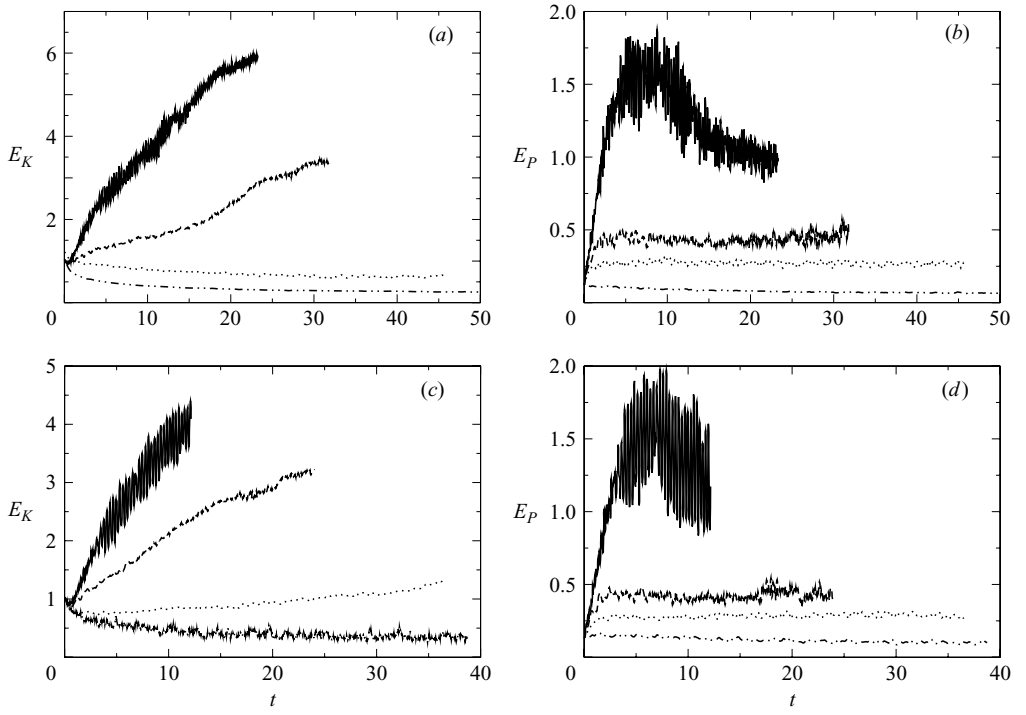

FIGURE 5. The time evolution of (*a*) the kinetic energy $E_K/(PL_h)^{2/3}$ and (*b*) potential energy $E_P/(PL_h)^{2/3}$. ——, Ad1; – – –, Ad2; · · · · ·, Ad3; —·—·—, Ad4. The time evolution of (*c*) the kinetic energy $E_K/(PL_h)^{2/3}$ and (*d*) potential energy $E_P/(PL_h)^{2/3}$. ——, Cd1; – – –, Cd2; · · · · ·, Cd3; —·—·—, Cd4.

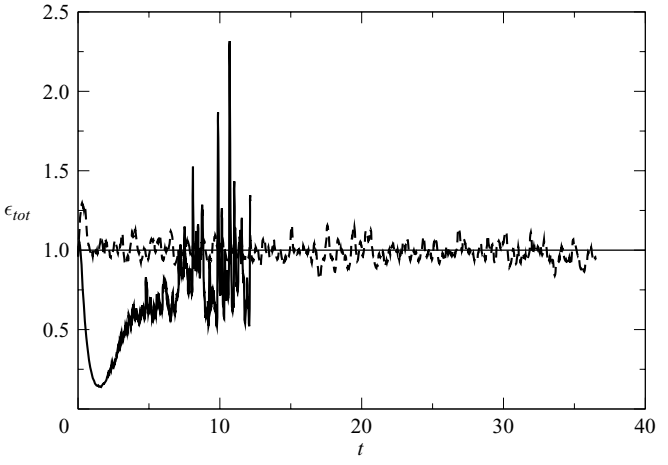

FIGURE 6. The time evolution of the sum of the kinetic and potential energy dissipation $(\epsilon_K + \epsilon_P)/P$. ——, Cd1; – – –, Cd3.

runs with forcing at $k_v' = 1$ reach a stationary state in which dissipation is equal to energy injection. In figure 6(*a*), we see the time evolution of total dissipation from run Cd1, with $k_v' = 1$. The dissipation is calculated as in Lindborg (2006). Typically, the dissipation is a little less than unity. Moreover, there are rather large intermittent

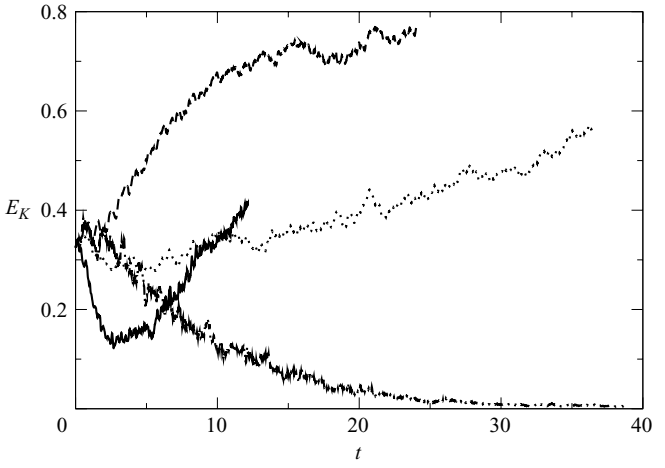

FIGURE 7. The time evolution of the kinetic energy in the shear mode normalized with the total kinetic energy. ———, Cd1; — — —, Cd2; · · · · ·, Cd3; —·—··—, Cd4.

bursts of high-amplitude dissipation, possibly a result of localized wave breaking events. This curve can be compared with the dissipation curve of run Cd3, with $k_v' = 5$, also shown in figure 6. In this run, a statistically stationary state is reached quite fast, in which dissipation fluctuates around unity, which means that there is a balance between power input and dissipation. It was also found that the evolution of kinetic energy in modes for which $k_\rho = 0$, so-called 'shear modes', is strongly dependent on the vertical forcing wavenumber. In runs with small k_v' we generally see an increase of energy, while in runs with large k_v' we see a decrease of energy in shear modes. This is illustrated in figure 7 where we have plotted the time evolution of kinetic energy in the shear modes from the Cd-runs. It has been observed in several recent numerical studies (Smith & Waleffe 2002; Laval, McWilliams & Dubrulle 2003; Waite & Bartello 2004, 2006) that a substantial amount of energy often accumulates in the shear modes and in many cases this accumulation continues through the whole simulation, so that a stationary state is not reached. Our results show that this growth increases significantly with decreasing vertical forcing wavenumber, which suggests that the growth of energy in shear modes is a characteristic feature of the regime $F_v \to 0$, but not of the regime $\{F_h \to 0, F_v \sim 1\}$.

In table 1, F_h is listed for all runs and F_v is listed for all d-runs. The Froude numbers are calculated as $F_v = uk_v^f/N$ and $F_h = uk_\rho^f/N$, where $u = \sqrt{E_K}$ and E_K is the mean kinetic energy. The value of u was obtained from the end state of each run. As we can see, $F_h \ll 1$ in all runs. For the d-runs with forcing at $k_v' = 1$, F_v is generally smaller than unity, while in the other d-runs we generally have $F_v \approx 1.0$, with some variations. This is illustrated in figure 8, where we have plotted the time evolution of F_v for the Cd-runs. This time evolution of F_v suggests that the flow adjusts to a state where $F_v \sim 1$.

Similar layered structures to those we saw in the r-runs also develop in the d-runs. However, the thickness of the layers is determined by the vertical forcing wavenumber, rather than the inherent dynamics of the Boussinesq equations. This is clear from figure 1. As already pointed out, figure 1(*a*) shows a horizontal velocity component in a vertical plane from run Cr. Figure 1(*b–e*) shows corresponding plots from runs Cd1–Cd4, which are forced in successively larger vertical wavenumbers. The thickness

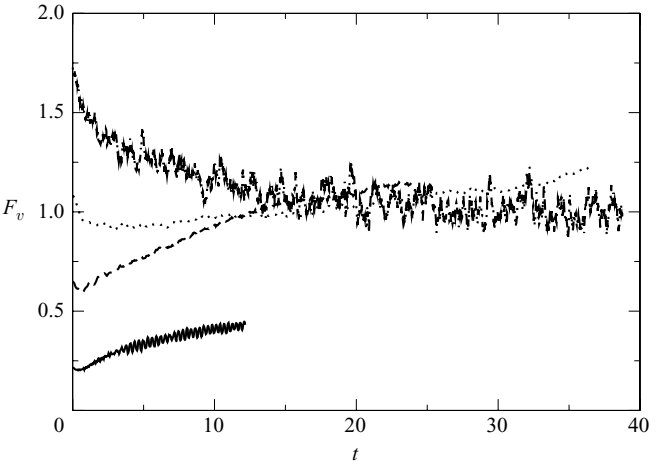

FIGURE 8. Time evolution of F_v for C-runs. Symbols are the same as in figure 7.

of the layers which can be observed in each plot corresponds to the vertical forcing wavenumber in each run. Comparing the four plots from the d-runs with the plot from the r-run, we see that the d-run that is most similar to the r-run is Cd3 with forcing at $k_v' = 5$. The results from this run were in all respects very similar to the results from the r-run. The same type of observation can also be made for the other sets of runs. By adjusting the vertical forcing wavenumber so that it corresponds to the 'natural' vertical length scale which we observe in the r-run we can produce the same type of dynamics in a d-run as in the r-run.

In figure 9 we see the compensated and normalized two-dimensional horizontal kinetic and potential energy spectra from runs Cd1–Cd4. The kinetic energy spectra are also divided into the spectra of rotational and divergent modes. At low wavenumbers the divergence spectra are larger in magnitude than the rotational spectra because forcing is applied in divergent modes. In all cases, the spectra show a $k_\rho^{-5/3}$-dependence and in all runs, except run Cd4 with forcing in $k_v' = 8$, the normalized kinetic and potential energy spectra fall on top of each other. Run Cd4 is unusual in that the vertical forcing wavenumber is fairly large, producing layered structures with a thickness (see figure 1*e*) which is smaller than the 'natural' layer thickness of the layers in run Cr (see figure 1*a*). In run Cd1 with forcing in $k_v' = 1$ the divergent mode spectrum is larger in magnitude than the rotational mode spectrum, while in runs Cd2 and Cd3 kinetic energy is approximately equipartitioned between divergent and rotational modes in the inertial range. This is similar to what we obtained in the r-runs. However, the magnitude of the normalized spectra decreases with increased vertical forcing wavenumber k_v, which means that the constants C_1' and C_2' are different for each run. It should be noted, however, that the runs Cd1 and Cd2 have not reached a stationary state when we stop them. So the fact that the normalized spectra from these are larger in magnitude than the spectra from the r-run may be a result of the lack of stationarity. In run Cd3, where the vertical forcing wavenumber matches the 'natural' layer thickness observed in the Cr-run, the two-dimensional horizontal spectra are very similar to the spectra from the Cr-run, with approximately the same magnitude in the inertial range. The same type of observation can be made for the other sets of simulations. In figure 10, we see the compensated and normalized two-dimensional horizontal spectra from runs Dd1 and

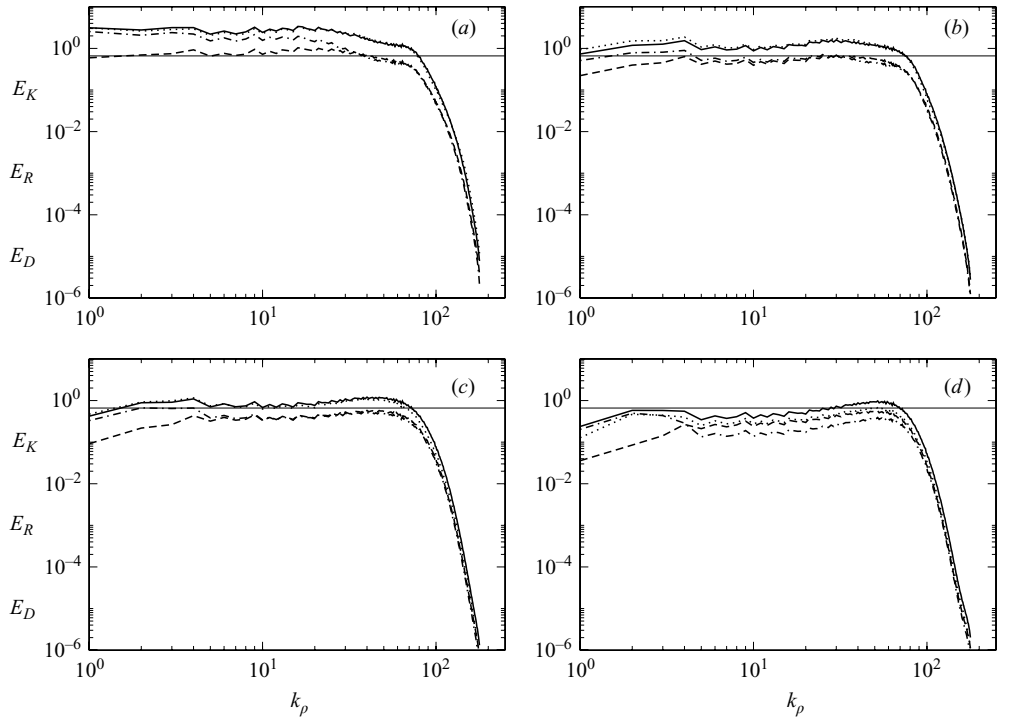

FIGURE 9. The compensated horizontal two-dimensional spectra, extracted from (*a*) run Cd1, (*b*) Cd2, (*c*) Cd3 and (*d*) Cd4. Lines as in figure 3.

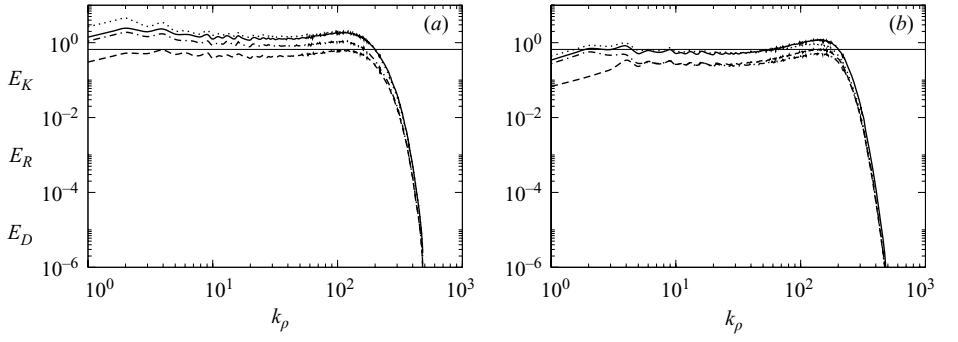

FIGURE 10. The compensated horizontal two-dimensional spectra, extracted from (*a*) run Dd1 and (*b*) Dd3. Lines as in figure 3.

Dd3. The spectra from both runs show a $k_\rho^{-5/3}$-dependence. However, the spectra from run Dd1, with forcing applied in $k_v' = 1$, is larger in magnitude and there is more energy in divergent modes than in rotational modes in the $k_\rho^{-5/3}$-range. Like run Cd1, Dd1 does not reach a stationary state and F_v is considerably smaller than in the runs with larger vertical forcing wavenumber k_v'. The spectra from run Dd3 with $k_f' = 4$, on the other hand, are very similar to the spectra from run Dr. The compensated kinetic and potential energy spectra fall on top of each other. There is equipartition of kinetic energy between divergent and rotational modes in the inertial range, and we find that $C_1' \approx C_2' \approx 0.66$, just as in run Dr.

3.1. *Frequency spectra from individual Fourier modes*

The most straightforward way to detect internal gravity waves is to calculate frequency spectra of divergent and potential energy from individual Fourier modes. If waves are present such spectra should show distinctive peaks at the internal wave frequency

$$\omega_{iw} = \frac{Nk_\rho}{\sqrt{k_\rho^2 + k_z^2}} = \frac{N\alpha}{\sqrt{1+\alpha^2}}, \tag{3.3}$$

where $\alpha = k_\rho/k_z$. Waves can be expected to be more prevalent in modes where the aspect ratio, α, is of the order of unity or larger than in modes with a very low aspect ratio. Our simulations are deliberately designed so that the aspect ratio for most modes is quite small, since the height of our boxes generally is much smaller than the width. To investigate the presence of waves in a continuous range of aspect ratios we have performed a simulation using the same parameters as in the Ar-run, except that we have extended the vertical side of the box by a factor of eight. We call this run $\mathrm{Ar_{ex}}$. This simulation also serves as a check that the dynamics is not significantly changed with a thicker box. We found that the horizontal spectra from run $\mathrm{Ar_{ex}}$ were almost indistinguishable from the spectra from run Ar, indicating that the dynamics in these two runs were very similar. We have calculated frequency spectra of rotational, divergent and potential energy from a large number of individual Fourier modes for run $\mathrm{Ar_{ex}}$, varying k_ρ and α. In order to obtain good statistics we have averaged the spectra over shells: $k_\rho \in [n-1/4, n+1/4]$, for different integer values of n. In general, we find that waves are more accentuated in modes with low values of k_ρ, corresponding to large horizontal scales in the box, and in modes where the aspect ratio is not too small. In high-wavenumber modes with low aspect ratio there are no waves present at all. To illustrate that the wave–vortical decomposition is valid for low-wavenumber modes, we plot the spectra from the mode $k_\rho = 1$, $\alpha = 1/4$ in figure 11(*a*). As we can see, the divergent and potential energy spectra both have a clear peak at the internal wave frequency and there is also equipartition between divergent and potential energy near the peak, which should be the case for internal gravity waves. The rotational energy spectrum, on the other hand, does not show any peak at the internal wave frequency. Most of the rotational energy is contained in frequencies which are much smaller than ω_{iw}. In figure 11(*b*) we see the frequency spectra of divergent energy for $k_\rho = 1$ and different α. The peak at the internal wave frequency is visible for all α, even for such a low value as $\alpha = 1/20$. However, the peak becomes broader with decreasing α. We can compare this figure with figure 11(*c*), where we have plotted the divergence frequency spectra for $k_\rho = 20$ and different α. For $\alpha = 1$ there is indeed a peak at ω_{iw}, but it is quite broad. For $\alpha = 2/5$, the peak has already shifted towards higher frequencies and broadened so much that it is questionable if there are any internal waves in this mode. For $\alpha = 1/5$, there is no sign of any peak. In figure 11(*d*) we have plotted the rotational frequency spectrum together with the divergence frequency spectrum for this mode. As can be seen, these two spectra fall on top of each other and most of the energy is contained in frequencies which are a little larger than ω_{iw}. Our interpretation of the frequency spectra which we have calculated from a large number of individual modes, of which we have presented a selection, is that waves become less and less prevalent as the cascade goes downscale. In the inertial range, there are only weak signs of waves and in the most dynamically important low-aspect-ratio modes there are no waves at all. In these modes, frequency spectra of rotational and divergent modes fall on top of each other.

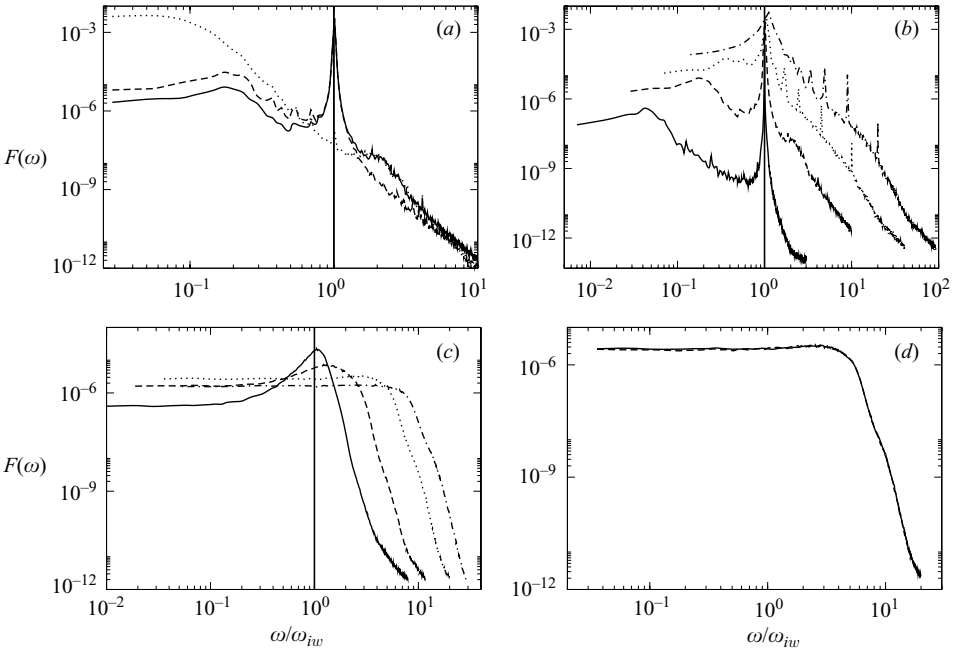

FIGURE 11. Frequency energy spectra from run $\mathrm{Ar_{ex}}$. (*a*) $k_\rho = 1$, $\alpha = 1/4$; ———, divergent; — — —, buoyant; · · · · ·, rotational mode; (*b*) $k_\rho = 1$, divergent modes; ———, $\alpha = \infty$; — — —, $\alpha = 1/4$; · · · · ·, $\alpha = 1/10$; —·—·—, $\alpha = 1/20$; (*c*) $k_\rho = 20$, divergent modes; ———, $\alpha = 1$; — — —, $\alpha = 2/5$; · · · · ·, $\alpha = 1/5$; —·—·—, $\alpha = 2/15$; (*d*) $k_\rho = 20$, $\alpha = 1/5$; ———, divergent; — — —, rotational mode.

4. Comparison with observational data

Many observational studies (e.g. Vinnichenko 1970; Nastrom *et al.* 1984; Cho, Newell & Barrick 1999; Lindborg 1999) show kinetic and potential mesoscale energy spectra of the form $k^{-5/3}$ in the upper troposphere and lower stratosphere. Recent numerical simulations (Koshyk & Hamilton 2001; Skamarock 2004; Kitamura & Matsuda 2006; Takahashi, Hamilton & Ohfuchi 2006) have been able to reproduce such mesoscale energy spectra. Koshyk & Hamilton (2001) argued on the basis of their simulation results that the mesoscale motions are undergoing a forward energy cascade and Cho & Lindborg (2001) drew the same conclusion on the basis of structure function measurements from aircraft data. Lindborg (2006) suggested that stratified turbulence with an associated forward energy cascade may be the dynamic origin of the observed spectra. Koshyk & Hamilton (2001) found that kinetic energy was approximately equipartitioned between rotational and divergent modes in their simulated mesoscale spectra. Lindborg (2007) analysed structure functions calculated from aircraft data in the upper troposphere and lower stratosphere (Lindborg 1999) and showed that the energy content in rotational and divergent modes are of the same order of magnitude in the mesoscale range. The present simulation results are consistent with these observations and thus give additional support to the stratified turbulence interpretation of the mesoscale energy spectra of the upper troposphere and lower stratosphere.

In this study, we have found that the forward energy cascade of stratified turbulence may not only be produced by forcing in rotational modes but also by forcing in divergent modes, provided that the forcing does not excite motions which violate

the condition $F_v \approx 1$. This result suggests that this type of turbulence may also be frequently prevalent in the ocean where excitation of internal gravity waves by wind surface forcing and bottom drag are supposed to be dynamically very important. It may also be the case that a substantial fraction of the energy which is injected by wind and tidal forcing into large-scale quasi-geostrophic rotational modes is transferred to smaller scales, as suggested by the very nice observational study of Scott & Wang (2005). Regardless of the nature of the forcing we can expect to see the formation of a downscale cascade of stratified turbulence with an inertial range starting at some horizontal wavenumber. This wavenumber may be different from case to case, depending on the nature of the forcing. However, a characteristic feature of stratified turbulence is that the advection term including the vertical velocity is of leading order in the dynamic equation and this cannot be the case in the quasi-geostrophic limit. Therefore, a lower limit of the smallest horizontal wavenumber of the forward energy cascade is set by the Rossby deformation radius.

Oceanic wavenumber spectra corresponding to spatial scales between ten and a couple of hundred metres in the vertical and between a couple of hundred metres and ten kilometres or more in the horizontal are generally interpreted as spectra of linear or weakly nonlinear internal gravity waves (Garret & Munk 1972, 1975, 1979). The average Richardson number in what is supposed to be the internal wave field is often of the order of unity (Munk 1981). The average Richardson number is here defined as

$$Ri = \frac{N^2}{\left\langle \dfrac{\partial u}{\partial z}\dfrac{\partial u}{\partial z} \right\rangle}, \tag{4.1}$$

where $\langle \ldots \rangle$ is a space–time-scale average over all motions in the wavenumber band of interest. The typical vertical Froude number corresponding to a certain vertical wavenumber band can be estimated in terms of the average Richardson number as

$$F_v \sim Ri^{-1/2}. \tag{4.2}$$

As we can see in table 1, we found $Ri \approx 1$ in our simulations. The inverse of the average Richardson number corresponding to a certain wavenumber band can be calculated by integration of the vertical shear spectrum. In figure 12, we have plotted the normalized shear spectra from four of our runs together with data points from Gargett *et al.* (1981), from different measurements in the interior of the ocean. In these studies the Ozmidov wavenumber, $k_b = 1/l_O$, was measured to about 1 c.p.m. (cycles per metre). The observational shear spectra thus correspond to vertical scales between 1 and 100 m and our simulated shear spectra would correspond to vertical scales from about 10 to 100 m. In the figure, we have also plotted a line corresponding to a non-normalized spectrum of the form $cN^2k_v^{-1}$, with $c = 0.75$. It is interesting to note that the observational spectra also give a Richardson number of the order of unity when they are integrated, either over the wavenumber band [0.01 0.1] c.p.m. (corresponding to wavelengths between 10 and 100 m) or over the wavenumber band [0.1 1] c.p.m. (corresponding to wavelengths between 1 and 10 m). We can thus make the estimate $F_v \sim Ri^{-1/2} \approx 1$ in both these wavenumber bands. This leads us to the suggestion that stratified turbulence of the type we have seen in this study can make an important contribution to oceanic dynamics at vertical scales up to at least 100 m. This would imply that the horizontal kinetic and potential energy wavenumber spectra sometimes should be of the form (1.5) and (1.6) in a wavenumber range corresponding to much larger horizontal wavelengths, presumably from about 10 or 100 m up to about 10 km. To

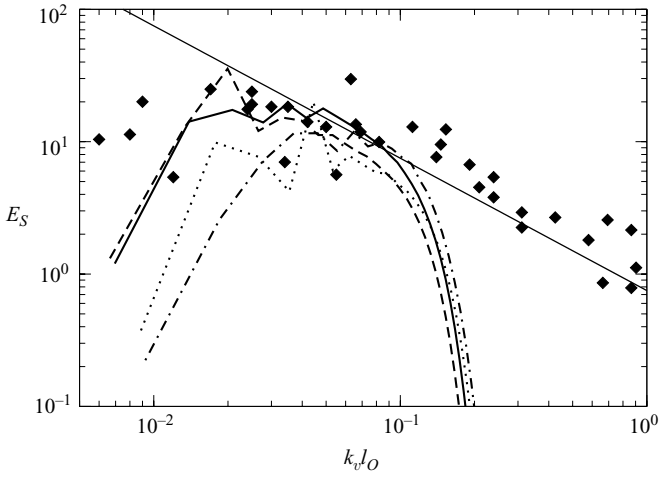

FIGURE 12. Vertical wavenumber spectra of vertical shear measured in the ocean (symbols; reproduced from Gargett *et al.* 1981) and extracted from the simulations (lines). ———, run Dr; — — —, run Dd2; —·—·—, run Cr; · · · · ·, run Cd3. The spectra are normalized by $(\epsilon N)^{1/2}$ and the wavenumber is normalized by l_O. The straight line represents the k_v^{-1} slope.

investigate if this is consistent with observations we have searched the literature for reported measurements of oceanic horizontal energy spectra. We have found no reports which are inconsistent with the stratified turbulence interpretation and we have found several reports which are fully consistent. Here, we will briefly review some of these.

Most measured horizontal spectra from the ocean are temperature spectra or potential energy spectra derived from temperature spectra, using the assumption that vertical displacements of fluid particles are isothermal. Most measurements were made in the 1960s and the 1970s. In figure 13 we have reproduced the horizontal potential energy spectra constructed by Dugan, Morris & Okawa (1986) from different measurements at different locations in the oceans, most of which having been reported elsewhere in the literature. For comparison we have also inserted a straight line representing a curve of the form $k_h^{-5/3}$. The line captures the general trend of the spectra quite well; in particular, in the middle range of wavenumbers corresponding to wavelengths between 100 m and 10 km or more, the measured spectra are consistent with a power law of the form in equation (1.6). Fitting the spectrum to the form (1.6) in this range and assuming that $\epsilon_P \sim \epsilon_K$ we can make the estimate $\epsilon = \epsilon_K + \epsilon_P \approx 10^{-9}\,\mathrm{m^2\,s^{-3}}$, which is consistent with typical values of the mean dissipation rate below the mixed layer in the ocean (see e.g. Gregg & Sanford 1988). The data points represented by dots in the middle range of wavenumbers are from measurements by Katz (1973). Katz divides his measured spectra into two regions. In the lower-wavenumber region, for wavenumbers between 0.01 and 1.0 c.p.km (cycles per km), he finds that the spectra have power-law form k^{-n} with n between 1.20 and 1.79, with a mean value of 1.54. Given the experimental accuracy, this is compatible with $n = 5/3$. For larger wavenumbers he finds that the spectra have a power-law form with $n = 2.3$. Katz compares his results with the k_h^{-2} model spectrum of Garret & Munk (1972) and concludes that his spectra are consistently more shallow than this for wavenumbers smaller than 1 c.p.km. He also points out that some previous measurements have given similar results.

Voorhis & Perkins (1966) measured temperature wavenumber spectra and structure functions in the near-surface thermocline in a region 200 km northwest of Bermuda.

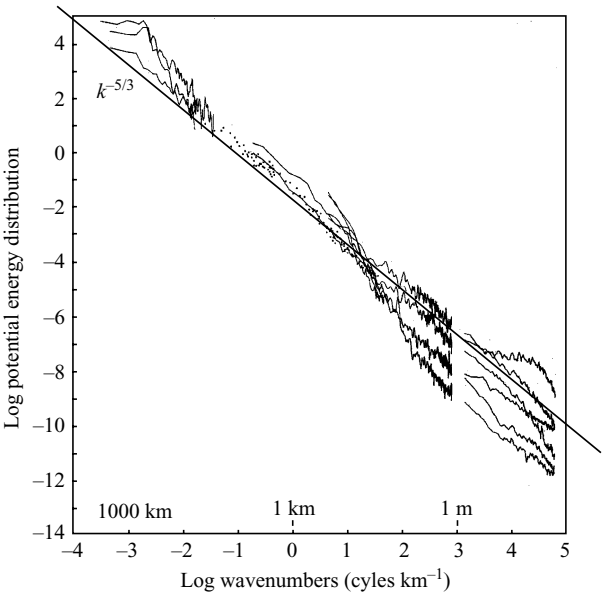

FIGURE 13. Horizontal wavenumber spectra of available potential energy in the ocean, collected from different observations. Reproduced from Dugan *et al.* (1986). We have inserted a straight line representing a $k_h^{-5/3}$-curve.

A thermistor mounted on a cable was towed at mean depth of 99 m around a star-shaped pattern, so that spectra could be measured along tracks with different orientation. Garret & Munk (1972) reference their measurements as giving support for their suggestion that the spectrum should fall off as k_h^{-2}. Voorhis & Perkins' own interpretation, however, is that they have measured a $k^{-5/3}$-spectrum. Moreover, they also report measurements of the horizontal temperature structure function, and these give even stronger support for the $k_h^{-5/3}$-interpretation. If the temperature spectrum falls off as $k^{-5/3}$ in a certain wavenumber range, then the horizontal temperature structure function should grow as $\rho^{2/3}$ in the corresponding range of separations ρ (Monin & Yaglom 1975). The horizontal temperature structure function, $\langle \delta T \delta T \rangle$, is the mean of the square of the difference, δT, between the temperatures at two points at the same depth whose relative horizontal separation distance is ρ. If the potential energy spectrum has the form (1.6), and if we make the common assumption that particle displacements are approximately isothermal, then the temperature structure function should have the form

$$\langle \delta T \delta T \rangle = \frac{T_z^2}{N^2} C_2'' \epsilon_P \epsilon_K^{-1/3} \rho^{2/3}, \tag{4.3}$$

where T_z is the vertical mean temperature gradient and (see Monin & Yaglom 1975)

$$C_2'' = \frac{4\pi}{\Gamma\left(\frac{5}{3}\right)\sqrt{3}} C_2 \approx 8.0\, C_2. \tag{4.4}$$

In figure 14 we have reproduced the temperature structure function given by Voorhis & Perkins. As can be seen, the data points follow the curve $\rho^{2/3}$ very closely in a range of separations between 100 m to 10 km. This is perhaps the strongest piece of evidence that there may be a stratified turbulence cascade range in the ocean. Voorhis & Perkins give the value $T_z = 0.02\,\mathrm{K\,m^{-1}}$ for the mean vertical temperature gradient.

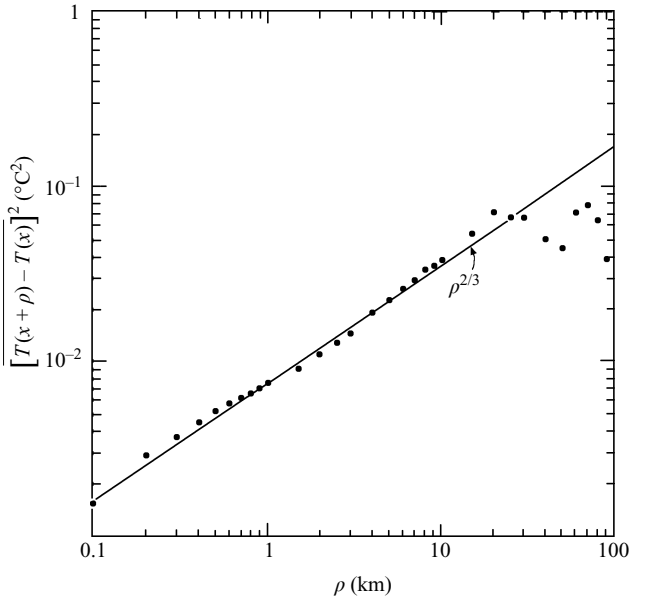

FIGURE 14. Horizontal temperature structure function reproduced from Voorhis & Perkins (1966).

From their figure 1, we can estimate the value of the buoyancy frequency to be $N = 0.02\,\mathrm{s}^{-1}$. Assuming that $\epsilon_P = 0.4\epsilon_K$ and $C_2 = 0.5$, using (4.3) and (4.4) and the values from figure 14, we obtain the estimate $\epsilon \approx 3 \times 10^{-7}\,\mathrm{m}^2\,\mathrm{s}^{-3}$. This is indeed higher than what is normally measured in the thermocline. The measurements are made in a rather active region in the upper summer thermocline, however, and therefore the estimated value of ϵ is not unreasonably high.

Similar results, however with somewhat more spread, have been reported by Black & Gluckman (1965), who measured temperature structure functions in the range of separation between 100 m and 20 km at different depths in the northern Atlantic. They found that the measured structure functions could be fitted to power laws ρ^n, with n varying between 1/2 and 4/5 and most values usually being close to 2/3. Williams (1968) measured temperature structure functions at depths 30 m, 60 m and 90 m in the open ocean. At 30 m and 60 m he found structure functions exhibiting two power-law ranges: $\rho^{1.1}$ at separations below a couple of hundred metres and $\rho^{2/3}$ from a couple of hundred metres up to 10 km. At the depth 90 m he only found the $\rho^{1.1}$-range. Williams points out that his results are consistent with the measurements by Lafond & Lafond (1967), who measured the thermal structure of the upper 240 m in the Pacific ocean using large arrays of thermistors mounted on chains which were towed behind a ship. Lafond & Lafond plot two average displacement spectra, one in the shallow isotherm 13° C in the main thermocline, and one in the deep thermocline 12° C. Each spectrum is averaged from twenty five data sets. They are given as frequency spectra calculated from the time series of temperature recorded on a moving ship. Given the speed of the ship the frequency range can be translated to a wavenumber range of a couple of hundred metres up to about 10 km. Both the spectra are consistent with a $k^{-5/3}$-dependence, as is also pointed out by Lafond & Lafond and indicated in their figure.

Very few recent measurements of horizontal wavenumber spectra in the ocean are reported in the literature, especially in the wavenumber range which is of particular interest for us in this study. Solievev, Lukas & Hacker (2000) report measurements of kinetic and potential energy spectra in the depth range from 20 to 250 m in the western equatorial Pacific. The measurements have a great advantage over previous measurements in that both velocity and density fluctuations have been measured, so the spectra are really the spectra of kinetic and potential energy. The wavenumber range is rather narrow, however, and furthermore it is just at the larger limit of the range which is of particular interest for us. The smallest wavelength is just below 10 km and the largest is just below 100 km. Solievev *et al.* interpret their spectra in the framework of the Garret & Munk internal wave model. However, the slope of the spectra is very close to 5/3 and they can equally well be interpreted as the spectra of stratified turbulence. Hollbrook & Fer (2005) have recently calculated potential energy spectra from seismographic data records of the interior density field from the ocean. They plot two spectra: the first is calculated from data taken quite near the coast. This spectrum exhibits a very nice $k^{-5/3}$-range at wavelengths from about 100 m to several kilometres. The authors interpret this spectrum as one of classical Kolmogorov turbulence, but we find that stratified turbulence is a more reasonable explanation. The other spectrum is taken quite far away from the coast and the authors interpret it as a gravity wave spectrum. However, it is rather similar to the near-coast spectrum, having a slope which is very close to $-5/3$. It may be the case that stratified turbulence was an important dynamic agent also in this case. However, we cannot exclude the gravity wave explanation.

To measure the distribution of energy between rotational and divergent modes in the ocean is, of course, very difficult. Despite all the difficulties such a measurement was performed by Müller, Lien & Williams (1988). In the IWEX-experiment (Internal Wave Experiment, see Briscoe 1975) measurement probes were mounted on the edges of a large tetrahedron which was submerged in the ocean. With such a configuration velocity measurements can be conducted simultaneously at three different points at the same depth. At each depth the three points can be regarded as lying on a circle with diameter d. With the base of the tetrahedron facing the bottom of the ocean d will increase with increasing depth. Using the Gauss and Stokes integral theorems the area-averaged vertical vorticity, ω, and horizontal divergence, $\xi = \nabla_h \cdot \boldsymbol{u}$, can be estimated from the three simultaneous velocity measurements. Müller *et al.* measured the frequency spectra of the area-averaged vorticity and divergence and also calculated the variance of these quantities at different depths corresponding to different values of the diameter d. Clearly, there can be no contribution to this variance from scales which are considerably smaller than the diameter of the circle. It is therefore reasonable to interpret the diameter-dependent variance as a kind of filtered variance where the contribution from scales which are smaller than d is filtered out. If $\Psi(k_\rho) = k_\rho^2 E^R(k_\rho)$ and $\Phi(k_\rho) = k_\rho^2 E^D(k_\rho)$ are the wavenumber spectra of vertical vorticity and horizontal divergence we would thus have

$$\langle \omega\omega \rangle(d) \sim \int_0^{k_d} \Psi(k_\rho)\,\mathrm{d}k_\rho, \quad \langle \xi\xi \rangle(d) \sim \int_0^{k_d} \Phi(k_\rho)\,\mathrm{d}k_\rho, \tag{4.5}$$

where $\langle \omega\omega \rangle$ and $\langle \xi\xi \rangle$ are the measured variances and $k_d \sim 2\pi/d$.† In figure 15 we have

† Arne Johansson (private communication) suggested that from Nyquist's theorem it may be argued that we instead should have $k_d \sim \pi/d$. But this is of minor importance for the comparison we make in this study.

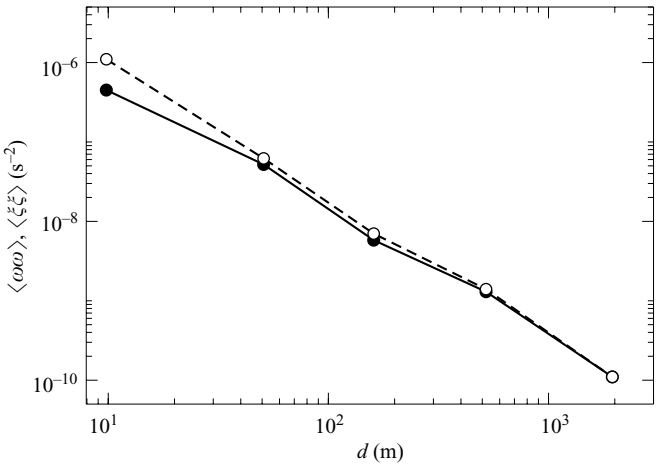

FIGURE 15. $\langle\omega\omega\rangle$ (black symbols, data; solid line connects the data points) and $\langle\xi\xi\rangle$ (open symbols, data; dashed line connects the data points) vs. the dimater d. Data from Müller *et al.* (1988).

plotted $\langle\omega\omega\rangle$ and $\langle\xi\xi\rangle$, using the values measured by Müller *et al.* Both curves fall off approximately as $d^{-5/3}$. If all measurements had been taken at the same depth this would correspond to energy spectra falling off as $E^R \sim E^D \sim k_\rho^{-4/3}$, which is also the spectral dependence inferred by Müller *et al.* (1988) under the assumption of vertical homogeneity. However, this assumption is questionable and there is therefore a large uncertainty attached to the estimated spectral dependence. What is more interesting is that the two curves in figure 15 are so close to each other. Especially in the range of diameters from 50 m up to 2 km they are very close to each other, indicating that kinetic energy is approximately equipartitioned between rotational and divergent modes at these scales. This is consistent with a stratified turbulence interpretation.

5. Summary and conclusions

We have performed a number of box simulations of strongly stratified turbulence forced in either rotational modes (r-runs) or divergent modes (d-runs). The r-runs confirmed the results already presented by Lindborg (2006). However, the parameters we chose for these runs are not exactly the same as used by Lindborg (2006) and we have not used exactly the same type of forcing scheme. We also used a completely different code. Moreover, we have generally used a larger number of resolution points in the vertical than was used by Lindborg (2006). In the r-runs the dynamics is dominated by spontaneous layer formation at vertical scale $l_v \sim u/N$ and a forward energy cascade in the horizontal, controlled by strong nonlinear interactions. A decomposition of the horizontal kinetic energy spectrum shows that kinetic energy is approximately equipartitioned between rotational and divergent modes in the inertial range, although the forcing is applied exclusively in rotational modes. This suggests that there are strong nonlinear interactions between the two types of modes and that their dynamics develop on a single time scale. Frequency energy spectra from individual Fourier modes with horizontal wavenumber in the inertial range show few signs of internal gravity waves and in relatively low-aspect-ratio modes there were no such signs whatsoever. Rotational and divergence energy spectra fall on top of each other in these modes. For aspect ratios of the order of unity waves are becoming less and less prevalent for increasing k_ρ, that is as the cascade is going downscale. In the

asymptotic limit of a very broad inertial range we expect to see no wave dynamics at all in stratified turbulence.

The d-runs results were quite similar to the r-runs. However, an important difference is that the vertical length scale is imposed by the vertical forcing wavenumber, k_v' , in the d-runs. In the runs with $k_v' = 1$, internal gravity waves dominated the dynamics in the largest possible wavelengths in the box and there was a constant increase of energy throughout the simulations. Moreover, there was a substantial growth of energy in shear modes ($k_\rho = 0$) in these runs. Shear modes represent all horizontal structures that do not fit into the box. A growth of energy in shear modes can therefore be interpreted as a tendency of the flow to form layers with a larger horizontal extent than the box. An interesting question is whether these layers would grow indefinitely or grow to a finite width if the same simulation were repeated with a much wider box. On this matter, we can, of course, only speculate, but we find it very likely that the layers would grow to a finite width. In stratified turbulence, the horizontal length scale can be estimated using the classical Taylor (1935) relation

$$l_h \sim \frac{u^3}{\epsilon}. \tag{5.1}$$

In order to reach a statistically stationary state with $\langle \epsilon \rangle = P$, the horizontal side of the box would thus need to be larger than u^3/P. Assuming also that the flow must satisfy the relation $F_v \approx 1$, we obtain the condition

$$\frac{L_x P \left(k_v^f\right)^3}{N^3} \geqslant 1 \tag{5.2}$$

for the flow to reach a stationary state. In table 1, we have listed the non-dimensional number on the left-hand side of (5.2) for all d-runs. This condition is seen to differentiate the d-runs that do reach a stationary state from those that do not. The condition (5.2) only contains parameters which are determined from the start of a simulation. We suggest that it can be used in future simulations of stratified turbulence with forcing in vertical wavenumbers, to determine whether a simulation can be expected to reach a stationary state or not. For example, in order to reach a stationary state in a simulation with the same values of N, P and k_v^f as in run Cd1, the condition (5.2) suggests that we would have to make the box wider by a factor of thirty. Apart from a much wider box, we would also need a much longer simulation period in order to reach a stationary state.

A comparison with observational data indicates that stratified turbulence may be prevalent not only at atmospheric mesoscales but also in the ocean at vertical and horizontal scales which are traditionally thought to be dominated by internal gravity waves. Observations from the ocean show that three characteristic features of stratified turbulence are often found in this range of scales. First, the Richardson number calculated from oceanic shear spectra in the range of vertical wavenumbers up to 100 m is often of the order of unity, which is consistent with $F_v \sim 1$. Second, horizontal potential energy spectra in the wavenumber range from 10 or 100 m up to several kilometres often show an approximate $k^{-5/3}$-dependence and temperature structure functions have been found to show a corresponding $\rho^{2/3}$-dependence. Third, rotational and divergent modes have been observed to contain approximately the same amount of energy in this range of scales, which is consistent with a stratified turbulence interpretation. We do not claim that these three similarities constitute a full proof that the dynamics of the ocean at these scales is dominated by stratified turbulence rather

than internal waves. However, the similarities are sufficiently interesting to motivate further observational studies.

As for the question raised in the introduction on whether stratified turbulence is a universal phenomenon whose dynamics is independent of the forcing mechanism, our results may be interpreted in two ways. On the one hand, the evolution of the d-runs showed a very large sensitivity to the vertical forcing wavenumber, and the magnitude of the horizontal energy spectra varied quite substantially between runs with different k_v'. In the runs with $k_v' = 1$, the divergent mode spectra were also larger in magnitude than the rotational mode spectra in the inertial range, contrary to what was found in the other runs. These results indicate that stratified turbulence can be sensitive to the forcing mechanism. On the other hand, all horizontal spectra showed approximate $k_\rho^{-5/3}$-dependence and the spectra from the d-runs that reached a stationary state were very similar to the spectra from the r-runs with an approximate equipartition of kinetic energy between rotational and divergent modes. These results indicate that stratified turbulence may indeed be a universal phenomenon. As long as the large-scale motions excited by the forcing satisfy $F_v \approx 1$, the inertial-range dynamics seems to be relatively independent of the type of forcing. Further studies are necessary to give a more complete answer to the question of universality.

We thank Jim Riley for many fruitful discussions about stratified turbulence. Financial support from the Swedish Research Council is gratefully acknowledged.

Appendix. Random forcing with constant energy injection rate in rotational or divergent modes

The flow is driven by a random volume force $\boldsymbol{f}$, implemented in Fourier space. The force is divergence free (in three dimensions) and applied either in rotational modes (r-runs) or horizontally divergent modes (d-runs). This is accomplished by using the Craya–Herring frame with the two principal unit vectors

$$\boldsymbol{e}^1(\boldsymbol{k}) = \frac{\boldsymbol{k} \times \boldsymbol{e}_z}{|\boldsymbol{k} \times \boldsymbol{e}_z|}, \tag{A 1}$$

$$\boldsymbol{e}^2(\boldsymbol{k}) = \frac{\boldsymbol{k} \times (\boldsymbol{k} \times \boldsymbol{e}_z)}{|\boldsymbol{k} \times (\boldsymbol{k} \times \boldsymbol{e}_z)|}, \tag{A 2}$$

where $\boldsymbol{k}$ is the wave vector and $\boldsymbol{e}_z$ is the unit vector in the vertical direction. It can be shown that $\boldsymbol{e}^1$ and $\boldsymbol{e}^2$ determine the principal directions in Fourier space of rotational and divergent modes respectively. The Fourier-transformed force, $\hat{\boldsymbol{f}}$, will therefore project onto $\boldsymbol{e}^1$ in r-runs and onto $\boldsymbol{e}^2$ in d-runs.

We require that the force injects energy into the system at a rate, P, which should be controllable and constant in time. The energy injection rate can be written as (Alvelius 1999)

$$P = \frac{1}{2} \sum \hat{\boldsymbol{f}} \cdot \hat{\boldsymbol{f}}^\star \Delta t + \frac{1}{2} \sum (\hat{\mathbf{u}} \cdot \hat{\boldsymbol{f}}^\star + \hat{\boldsymbol{f}} \cdot \hat{\boldsymbol{u}}^\star), \tag{A 3}$$

where Δt is the time step, * denotes the complex conjugate, $\hat{\mathbf{u}}$ is the Fourier-transformed velocity and the summations are taken over all wave vectors. If the force is random and uncorrelated with the velocity field, the second sum should be small, and ideally equal to zero in the case when forcing is applied in infinitely many modes. However, there is a problem here. Practically, forcing is, of course, applied in a finite number of modes. If the first sum is to make a finite contribution in the limit

$\Delta t \to 0$, the magnitude of the force has to scale as $|\hat{\boldsymbol{f}}| \sim (\Delta t)^{-1/2}$. Each term in the second sum will therefore scale as $(\Delta t)^{-1/2}$ and there is a risk that this sum will make a dominant contribution to the energy injection rate, even though the separate terms tend to cancel each other. The energy injection rate will then fluctuate substantially which can also lead to numerical problems. To avoid this, we design the forcing in such a way that the second sum in (A 3) is exactly equal to zero at each time step. The method is similar to the method developed by Alvelius (1999). However, whereas Alvelius required that each term in the second sum of (A 3) should be equal to zero, we require that they should cancel each other in pairs. The reason why we have to introduce this modification is that it is impossible to implement a two-dimensional random force in rotational modes using exactly the same method as Alvelius.

We let $\boldsymbol{k}_1$ and $\boldsymbol{k}_2$ be two wave vectors satisfying $k_{1_\rho} = k_{2_\rho}$ and $k_{1_z} = k_{2_z}$. We also let the projections of $\boldsymbol{k}_1$ and $\boldsymbol{k}_2$ onto the horizontal plane be orthogonal. For r-runs we write the force in these two modes as

$$\hat{\boldsymbol{f}}(\boldsymbol{k}_1) = \sqrt{S(k_\rho, k_z)}\exp(-\mathrm{i}\theta)\cos\phi\,\boldsymbol{e}^1(\boldsymbol{k}_1), \tag{A 4}$$

$$\hat{\boldsymbol{f}}(\boldsymbol{k}_2) = \sqrt{S(k_\rho, k_z)}\exp(-\mathrm{i}(\theta+\psi))\sin\phi\,\boldsymbol{e}^1(\boldsymbol{k}_2), \tag{A 5}$$

where ϕ and ψ are random angles, θ is an angle which will be determined from the condition that the second sum in (A 3) should be equal to zero and S is the amplitude, which we choose as

$$S(k_\rho, k_z) = A\frac{\exp\left(-\left(k_\rho - k_\rho^f\right)^2\right)\delta\left(|k_z| - k_v^f\right)}{2\pi k_\rho}. \tag{A 6}$$

Here, A is a normalization constant which is determined so that the injection rate becomes exactly equal to P, k_ρ^f is the horizontal forcing wavenumber and k_v^f is the vertical forcing wavenumber. For d-runs we write the forcing in the corresponding way, with $\boldsymbol{e}^1$ replaced by $\boldsymbol{e}^2$. In all runs we choose $k_\rho^f = 3$. In r-runs we only force in modes for which $0 < k_\rho \leqslant 3$ and in d-runs we only force in modes for which $0 < k_\rho \leqslant 5$. In r-runs we set $k_v^f = 0$ and in d-runs k_v^f is varied. The condition that the second sum in (A 3) should be equal to zero is satisfied by requiring that

$$\mathrm{Re}[\hat{\boldsymbol{u}}(\boldsymbol{k}_1)\cdot\hat{\boldsymbol{f}}^\star(\boldsymbol{k}_1) + \hat{\boldsymbol{u}}(\boldsymbol{k}_2)\cdot\hat{\boldsymbol{f}}^\star(\boldsymbol{k}_2)] = 0. \tag{A 7}$$

This condition gives an equation for the angle θ,

$$\tan\theta = \frac{\mathrm{Re}[\xi_1] + \mathrm{Re}[\xi_2]\cos\psi + \mathrm{Im}[\xi_2]\sin\psi}{-\mathrm{Im}[\xi_1] + \mathrm{Re}[\xi_2]\sin\psi - \mathrm{Im}[\xi_2]\cos\psi} \tag{A 8}$$

where

$$\xi_1 = \hat{\boldsymbol{u}}(\boldsymbol{k}_1)\cdot\boldsymbol{e}^1(\boldsymbol{k}_1)\cos\phi, \qquad \xi_2 = \hat{\boldsymbol{u}}(\boldsymbol{k}_2)\cdot\boldsymbol{e}^1(\boldsymbol{k}_2)\sin\phi \tag{A 9}$$

for r-runs. For d-runs we obtain the corresponding expressions where $\boldsymbol{e}^1$ is replaced by $\boldsymbol{e}^2$.

REFERENCES

Alvelius, K. 1999 Random forcing of three-dimensional homogeneous turbulence. *Phys. Fluids* **11**, 1880–1889.

Bartello, P. 1995 Geostrophic adjustment and inverse cascades in rotating stratified turbulence. *J. Atmos. Sci.* **52**, 4410–4428.

Billant, P. & Chomaz, J.-M. 2001 Self-similarity of strongly stratified inviscid flows. *Phys. Fluids* **13**, 1645–1651.

Black, C. F. & Gluckman, P. M. 1965 Large scale structure of turbulence beneath the mixed layer. *Trans. Conf. on Ocean Science and Ocean Engineering*, vol. 2, p. 687. Marine Technology Society, Washington, DC.

Brethouwer, G., Billant, P., Lindborg, E. & Chomaz, J.-M. 2007 Scaling analysis and numerical simulation of strongly stratified turbulent flows. *J. Fluid Mech.* (in press).

Briscoe, M. G. 1975 Preliminary results from the trimoored internal wave experiment (IWEX). *J. Geophys. Res.* **80**, 3872–3884.

Canuto, C., Hussaini, M. Y., Quarteroni, A. & Zhang, T. A. 1988 *Spectral Methods in Fluid Dynamics*, pp. 85–86, 205–206. Springer.

Cho, J. Y. N., Newell, E. & Barrick, J. D. 1999 Horizontal wavenumber spectra of winds, temperature and trace gases during the Pacific Exploratory Missions: 2. Gravity waves, quasi-two-dimensional turbulence and vortical modes. *J. Geophys. Res.* **104**, 16297–16308.

Cho, J. Y. N. & Lindborg, E. 2001 Horizontal velocity structure functions in the upper troposphere and lower stratosphere 1. Observations. *J. Geophys. Res.* **106**, 10223–10232.

Dewan, E. 1997 Saturated-cascade similitude theory of gravity wave spectra. *J. Geophys. Res.* **102**, 29799–29817.

Dugan, J. P., Morris, W. D. & Okawa, B. S. 1986 Horizontal wave number-distribution of potential energy in the ocean. *J. Geophys. Res.* **91**, 12993–13000.

Garret, C. & Munk, W. 1972 Space-time scales of internal waves. *Geophys. Fluid Dyn.* **2**, 225–264.

Garret, C. & Munk, W. 1975 Space-time scales of internal waves: A progress report. *J. Geophys. Res.* **80**, 291–297.

Garret, C. & Munk, W. 1979 Internal waves in the ocean. *Annu. Rev. Fluid. Mech.* **11**, 339–369.

Gargett, P. J., Hendricks, P. J., Sanford, T. B., Osborn, T. R. & Williams A. J. 1981 A composite spectrum of vertical shear in the open ocean. *J. Phys. Oceanogr.* **11**, 1258–1271.

Godeferd, F. S. & Cambon, C. 1994 Detailed investigation of energy transfers in homogenous stratified turbulence. *Phys. Fluids* **6**, 2084–2100.

Gregg. M. C. & Sanford, T. B. 1988 The dependence of turbulent dissipation on stratification in a diffusively stable thermocline. *J. Geophys. Res.* **93**, 12381–12392.

Hollbrook, W. S. & Fer, I. 2005 Ocean internal wave spectra inferred from seismic reflection transects. *Geophys. Res. Lett.* **32**, L15604, 1–4.

Kaneda, Y., Ishihara, T., Yokokawa, M., Uno, A. & Itakura, K. 2003 Energy dissipation rate and energy spectrum in high resolution direct numerical simulations of turbulence in a periodic box. *Phys. Fluids* **15**, L21–L24.

Katz, E. J. 1973 Profile of an isopycnal surface in the main thermocline of the sargasso sea. *J. Phys. Oceanogr.* **3**, 448–456.

Kitamura, Y. & Matsuda, Y. 2006 The k_H^{-3} and $k_H^{-5/3}$ energy spectra in stratified turbulence. *Geophys. Res. Lett.* **33**, LO5809.

Koshyk, J. N. & Hamilton, K. 2001 The horizontal kinetic energy spectrum and spectral budget simulated by a high- resolution troposphere-stratosphere-mesosphere GCM. *J. Atmos. Sci.* **58**, 329–348.

Lafond, E. C. & Lafond, K. G. 1967 Temperature structure in the upper 240 meters of the sea. *The New Thrust Seaward*, pp. 23–45. Marine Technological Society, Washington DC.

Lamorgese, A. G., Caughey, D. A. & Pope, S. B. 2005 Direct numerical simulations of homogeneous turbulence with hyperviscosity. *Phys. Fluids* **17**, 015106.

Laval, J.-P. McWilliams, J. C. & Dubrulle, B. 2003 Forced stratified turbulence: Succesive transition with Reynolds number. *Phys. Rev.* E **68**, 036308.

Lelong, M.-P. & Riley, J. J. 1991 Internal wave-vortical mode interactions in strongly stratified flows. *J. Fluid Mech.* **232**, 1–19.

Lindborg, E. 1999 Can the atmospheric kinetic energy be explained by two-dimensional turbulence? *J. Fluid Mech.* **388**, 259–288.

Lindborg, E. 2005 The effect of rotation on the mesoscale energy cascade in the free atmosphere. *Geophys. Res. Lett.* **32**, L01809.

Lindborg, E. 2006 The energy cascade in a strongly stratified fluid. *J. Fluid Mech.* **550**, 207–242.

Lindborg, E. 2007 Horizontal spectra of vertical vorticity and horizontal divergence in the upper troposphere and lower stratosphere. *J. Atmos. Sci.* (in press).

Monin, A. S. & Yaglom, A. M. 1975 *Statistical Fluid Mechanics II*. The MIT Press.

Müller, P., Lien, R.-C. & Williams, R. 1988 Estimates of potential vorticity at small scales in the ocean *J. Phys. Oceanogr.* **18**, 401–416.

Munk, W. 1981 Internal waves and small-scale processes. In *Evolution of Physcial Oceanogrophy* (ed. B. A. Warren & C. Wunsh), pp. 264–291. The MIT Press.

Nastrom, G. D. & Gage, K. S. & Jasperson, W. H. 1984 Kinetic energy spectrum of large- and mesoscale atmospheric processes. *Nature* **310**, 36–38.

Riley, J. J. & Lelong, M.-P. 2000 Fluid motions in the presence of strong stable stratification. *Annu. Rev. Fluid Mech.* **32**, 613–657.

Riley, J. J. & deBruynKops, S. T. 2003 Dynamics of turbulence strongly influenced by buoyancy *Phys. Fluids* **15**, 2047–2059.

Scott, R. B. & Wang, F. M. 2005 Direct evidence of an oceanic inverse kinetic energy cascade from satellite altimetry. *J. Phys. Oceanogr.* **35**, 1650–1666.

Skamarock, W. C. 2004 Evaluating Mesoscale NWP models using kinetic energy spectra. *Mon. Weath. Rev.* **132**, 3019–3032.

Smith, L. M. & Waleffe, F. 2002 Generation of slow large scales in forced rotating stratified turbulence. *J. Fluid Mech.* **451**, 145–168.

Soloviev, A., Lukas, R. & Hacker, P. 2000 Horizontal structure of the upper ocean velocity and density fields in the western pacific warm pool: depth range from 20 to 250 m. *J. Phys. Oceanogr.* **30**, 416–432.

Takahashi, Y. O., Hamilton, K. & Ohfuchi, W. 2006 Explicit global simulation of the mesoscale spectrum of atmospheric motions. *Geophys. Res. Lett.* **33**, L12812.

Taylor, G. I. 1935 Statistical theory of turbulence. *Proc. R. Soc. Lond.* A **151**, 421–478.

Waite, M. L. & Bartello, P. 2004 Stratified turbulence dominated by vortical motion. *J. Fluid Mech.* **517**, 281–308.

Waite, M. L. & Bartello, P. 2006 Stratified turbulence generated by internal gravity waves. *J. Fluid Mech.* **546**, 313–339.

Williams, R. B. 1968 Horizontal temperature variations in the upper water of the open ocean. *J. Geophys. Res.* **73**, 7127–7132.

Vinnichenko, V. K. 1970 The kinetic energy spectrum in the free atmosphere – 1 second to 5 years. *Tellus* **22**, 158–166.

Voorhis, A. D. & Perkins, H. T. 1966 The spatial spectrum of short-wave temperature fluctuations in the near-surface thermocline. *Deep-Sea Res.* **13**, 641–654.